Magnetic Resonance in Medicine 64:1078–1088 (2010)

A Rapid and Robust Numerical Algorithm for Sensitivity Encoding with Sparsity Constraints: Self-Feeding Sparse SENSE

Feng Huang,[1]* Yunmei Chen,[2] Wotao Yin,[3] Wei Lin,[1] Xiaojing Ye,[2] Weihong Guo,[4] and Arne Reykowski[1]

The method of enforcing sparsity during magnetic resonance imaging reconstruction has been successfully applied to partially parallel imaging (PPI) techniques to reduce noise and artifact levels and hence to achieve even higher acceleration factors. However, there are two major problems in the existing sparsity-constrained PPI techniques: speed and robustness. By introducing an auxiliary variable and decomposing the original minimization problem into two subproblems that are much easier to solve, a fast and robust numerical algorithm for sparsity-constrained PPI technique is developed in this work. The specific implementation for a conventional Cartesian trajectory data set is named self-feeding Sparse Sensitivity Encoding (SENSE). The computational cost for the proposed method is two conventional SENSE reconstructions plus one spatially adaptive image denoising procedure. With reconstruction time approximately doubled, images with a much lower root mean square error (RMSE) can be achieved at high acceleration factors. Using a standard eight-channel head coil, a net acceleration factor of 5 along one dimension can be achieved with low RMSE. Furthermore, the algorithm is insensitive to the choice of parameters. This work improves the clinical applicability of SENSE at high acceleration factors. Magn Reson Med 64:1078–1088, 2010. © 2010 Wiley-Liss, Inc.

Key words: partially parallel imaging; *g*-factor; sparsity constraint; prior information; compressed sensing; numerical algorithm

Partially parallel imaging (PPI) techniques (1,2) are being routinely used to achieve increased image resolution, decreased motion artifacts, and shorter scan time in magnetic resonance imaging (MRI). However, PPI techniques reduce acquisition time at the cost of a reduction in signal-to-noise ratio (SNR). With an increase in the acceleration factor, the increase in noise and artifact levels can become significant, thereby reducing the diagnostic quality of the image. To avoid significant artifacts and noise amplification, the acceleration factor, R, is typically restricted to values far below the theoretical limit (i.e., the number of coil elements). For example, acceleration factors are no more than 3 in most clinical exams for the widely available eight-channel head coil. To reduce the noise and artifact levels, techniques of enforcing sparsity in PPI reconstruction have recently been proposed (3–6), where "sparsity" means that the to-be-reconstructed image has a sparse representation in a known and fixed mathematical transform domain (7). These techniques enforce the sparsities of the to-be-reconstructed image in finite difference domain and wavelet transform domain by minimizing its total variation (TV) norm and the L_1 norm of its wavelet transform. The sparsity constraints play an important role in lowering the noise/artifact levels of the reconstructed images. Meanwhile, a data fidelity term is used to preserve image contrast and resolution. Sparsity constraints and data fidelity are balanced by the parameters that are the weights on the sparsity terms, called regularization parameters. Given optimal regularization parameters, ideal acquisition scheme, and sufficient reconstruction time, these sparsity-constrained methods can produce high-quality images with high acceleration factors. In Ref. (3), impressive reconstructions were presented with acceleration factor as high as 8 in 2D imaging using radial acquisition and a 12-channel head coil. Using a piece-wise constant phantom and vary-density random acquisition scheme, an acceleration factor of 8 was achieved with an eight-channel torso coil (4). Using 2D acceleration and Poisson-disc sampling, an acceleration factor of 5 (2.5×2) was achieved for 3D with a four-channel extremity coil (5). This previous work demonstrates that it is possible to achieve acceleration factors even higher than the number of coil elements when the to-be-reconstructed image is very sparse, such as with a piece-wise constant contrast or with very limited image support. However, aside from the difficulty of implementing these special acquisition trajectories in general applications, there are two intrinsic problems that have limited the clinical applicability of these advanced technologies: speed and robustness. In the literature, the conjugate gradient method (3,4,8) or the iterative convolution in *k*-space method (5,9) were used for implementation of sparsity constrained PPI. Except in Refs. (7) and (3), no reconstruction time information was explicitly reported for 2D images. In Ref. (7), without combining with PPI, the reconstruction for a single angiogram slice with matrix size 480×92 took about 30 sec in MATLAB®. In Ref.

[1]Advanced Concept Development, Invivo Corporation, Gainesville, Florida, USA.
[2]Department of Mathematics, University of Florida, Gainesville, Florida, USA.
[3]Department of Computational and Applied Mathematics, Rice University, Houston, Texas, USA.
[4]Department of Mathematics, Case Western Reserve University, Cleveland, Ohio, USA.
*Correspondence to: Feng Huang, Invivo Corporation, 3545 SW 47th Avenue, Gainesville, FL 32603 USA. E-mail: fhuang@invivocorp.com
Received 4 August 2009; revised 6 April 2010; accepted 18 April 2010.
DOI 10.1002/mrm.22504
Published online 17 June 2010 in Wiley Online Library (wileyonlinelibrary.com).

(3), the reconstruction time was in minutes for a 256 × 256 image acquired by a 12-elements coil (C/C++ using the GNU Scientific Library/Dell PowerEdge 2900 server with two Intel Xeon 5060 3.2 GHz dual core processors and 4 Gb memory). For 3D imaging, the sparsity regularized reconstruction could take hours (10). Such a prolonged reconstruction time is not acceptable for clinical applications.

Robustness is another potential problem with existing techniques. The final image quality is sensitive to the regularization parameters (3,11). An inappropriate regularization parameter can result in a significantly reduced spatial resolution or significant residual artifacts/noise. The optimal parameter is a function of, among other things, the subject, the acquisition sequences, and the acceleration factor. An optimal parameter-decision scheme that is generally applicable has not yet been published. Previous literature (3–6,8,10) used empirical values and did not provide extensive discussions on their parameter decision schemes.

The goal of this article is to tackle both the speed and robustness problems by using a novel numerical algorithm, hence improving the clinical applicability of sparsity constrained PPI with general-purpose imaging sequences. A fast algorithm for compressed sensing (CS) with single channel data has recently been introduced in (12), most of the single-channel compressed-sensing reconstruction can be completed in seconds but cannot be directly applied for sparsity-constrained PPI because the integration of sensitivity maps destroys the required operator orthogonality. One key concept in this fast algorithm is to decompose one complex problem into several subproblems that can be solved much faster by variable splitting. In this work, we adopt the idea of variable-splitting and apply the classical quadratic penalty technique to the constraint to improve the speed and robustness of sparsity constrained PPI.

THEORY

In this section, after the introduction of the general theory of the proposed numerical algorithm, a specific implementation for Cartesian data sets is provided. This specific implementation is named self-feeding Sparse SENSE.

Sparse Representation of MR Images

The goal of CS MRI is to accurately reconstruct an image from a small subset of *k*-space rather than a complete *k*-space data set in order to reduce scan time while preserving the image quality. The CS approach requires that: (a) the to-be-reconstructed image has a sparse representation in a known transform domain, (b) the aliasing artifacts due to *k*-space undersampling are incoherent (noise-like) in that transform domain, and (c) there exists a nonlinear reconstruction algorithm that can enforce the sparsity in the transform domain and preserve the consistency of the reconstruction using the acquired data. Recent study has shown that while MR images may not be sparse with respect to their pixel intensities, they are sparse in certain transform domains. These transforms are called sparsifying transforms. It has been shown in Ref. (7) that MR images may be sparse in its finite difference domain, and in its wavelet transformation domain. In that work, the authors proposed the following nonlinear scheme for MR image reconstruction with partially scanned data:

$$\min_I E(I) = \|F_p(I) - k\|_2^2 + \lambda\|\nabla I\|_1 + \mu\|\Psi(I)\|_1, \quad [1]$$

where $F_p(*)$ is the Fourier transform operator combined with the sampling mask (a matrix with value 1 at sampled locations and value 0 at other locations), k is the partially acquired data, I is the to-be-reconstructed image, ∇ is the gradient operator, $\Psi(*)$ is an optional sparsifying transform (e.g., a wavelet transform), and $\|*\|_1$ and $\|*\|_2$ denote the L_1 and L_2 norms. The nonnegative regularization parameters λ and μ balance these terms. The first term is the data fidelity term; it ensures the consistency of the reconstructed image with the acquired data. The remaining terms are sparsity constraints; they enforce the sparsity of the reconstructed image in its finite difference domain and wavelet transform domain, respectively. Using a random or pseudorandom acquisition trajectory, the sparsity constraints can reduce or remove the incoherent aliasing artifacts. Promising results have been achieved with significantly undersampled single-channel *k*-space data (10,13,14). Recently this model has been extended to use the sparsity in terms of a dictionary (15). Moreover, fast numerical methods (12,13,16–21) have been developed to efficiently solve the minimization problem. For instance, using the method in (12), a 256 × 256 two-dimensional (2D) image can be reconstructed on average in 1 sec.

PPI With Sparsity Constraints

There are great interests in combining the CS technique with PPI. A natural extension of model [1] from a single channel to multichannel imaging is as follows (6):

$$\min_I E(I) = \sum_{j=1}^{\mathrm{Nch}} \|F_p(S_j I) - k_j\|_2^2 + \lambda\|\nabla I\|_1 + \mu\|\Psi(I)\|_1. \quad [2]$$

Here, j is the coil count, Nch is the number of coil elements, S_j is the sensitivity map of the jth coil element, and k_j is the partially acquired data for the jth coil element. As a result of this combination, the final result can be better than that by PPI or CS-MRI (7) individually. It has been shown in (6) that an image with well-balanced SNR and spatial resolution can be obtained by minimizing the energy functional in [2]. Incorporating sensitivity maps from multiple channels helps balance data fidelity and regularization. However, due to the presence of sensitivity map S_j, the fast numerical algorithms developed in (12,16,18–21) for single-channel MRI reconstruction cannot be applied directly. This results in a much longer reconstruction time to solve model [2], which hinders its clinical applicability.

Decomposition of a Complex Problem into Two Easier Subproblems

A major contribution of this work is to provide a fast numerical algorithm to solve model [2]. Our method is

based on the variable-splitting and classic quadratic penalty technique in optimization to decompose the nonlinear minimization problem [2] into two subproblems, both of which can be solved in faster and more stable manners. We first introduce an auxiliary variable $\hat{I}$ to transfer I out of the terms of sparsity constraints (the last two terms) in [2], then we solve the following constrained minimization problem as an alternate:

$$\min_{I,\hat{I}} E(I,\hat{I}) = \sum_{j=1}^{\text{Nch}} \left\|F_p(S_jI) - k_j\right\|_2^2 + \lambda\left\|\nabla\hat{I}\right\|_1 + \mu\left\|\Psi(\hat{I})\right\|_1 \text{ s.t } \hat{I} = I. \quad [3]$$

Clearly, minimizing [2] and [3] are equivalent in the sense that they share the same solution. To solve [3], we relax the equality constraint and penalize its violation by quadratic function, then solve the following unconstrained minimization problem:

$$\min_{I,\hat{I}} E(I,\hat{I}) = \sum_{j=1}^{\text{Nch}} \left\|F_p(S_jI) - k_j\right\|_2^2 + \lambda\left\|\nabla\hat{I}\right\|_1 + \mu\left\|\Psi(\hat{I})\right\|_1 + \alpha^2\left\|I - \hat{I}\right\|_2^2. \quad [4]$$

With sufficiently large α, solving problem [4] gives an approximation of the solution to problem [3].

Now problem [4] can be solved iteratively by minimizing the energy functional in [4] with respect to I and $\hat{I}$ individually while keeping the other one fixed. That is, we solve the following two subproblems alternately until $(I,\hat{I})$ converge:

$$I\text{-subproblem: } \min_I E[I] = \min_I \sum_{j=1}^{\text{Nch}} \left\|F_p(S_jI) - k_j\right\|_2^2 + \alpha^2\left\|I - \hat{I}\right\|_2^2, \quad [5]$$

$$\hat{I}\text{-subproblem: } \min_{\hat{I}} E[\hat{I}] = \min_{\hat{I}} \lambda\left\|\nabla\hat{I}\right\|_1 + \mu\left\|\Psi(\hat{I})\right\|_1 + \alpha^2\left\|I - \hat{I}\right\|_2. \quad [6]$$

As two parameters are sufficient to balance the three terms in Eq. [6], α^2 can be set to be 1 without any influence on the final result. $\hat{I}$-subproblem is then modified to be

$$\hat{I}\text{-subproblem: } \min_{\hat{I}} E[\hat{I}] = \min_{\hat{I}} \lambda\left\|\nabla\hat{I}\right\|_1 + \mu\left\|\Psi(\hat{I})\right\|_1 + \left\|I - \hat{I}\right\|_2. \quad [7]$$

Now the nonlinear minimization problem [2], which takes longer to solve, has been decomposed to two subproblems, [5] and [7]. Equation [5] is the model for prior information $\hat{I}$ regularized PPI, which is a linear problem and is easier to solve. Equation [7] is the well-known total variation (TV) + wavelet image denoising problem, for which there have been a number of numerical methods (12,18,19,21–25) proposed to solve it with high efficiency and stability. This decomposition moves the most time-consuming terms, L_1 norm constraints, out of the multichannel system. The convergence behavior of the two subproblems [5] and [7] can be deduced and summarized in the following Theorem: For fixed $\alpha > 0$, the sequence

$$\left\{\left(I_n, \hat{I}_n\right)\right\}_n, \quad n = 0, 1, 2, \ldots,$$

generated by alternately solving Eqs. [5] and [7] from any starting point $(I_0,\hat{I}_0)$ converges to $(I^\alpha,\hat{I}^\alpha)$, a solution of [4], and the convergence rate is linear, that is,

$$\left\|I_n - I^\alpha\right\| \le C\theta^n\left\|I_0 - I^\alpha\right\|$$

for some $\theta \in (0,1)$, and a similar estimate for $\hat{I}_n$ for some $\hat{\theta} \in (0,1)$.

Self-Feeding Sparse SENSE

Equations [5] and [7] are applicable to acquired data sets with any trajectory. Pseudorandom trajectories are preferred for imaging with partially acquired data because the incoherent aliasing artifacts are easier to remove than coherent artifacts. However, in this work, we focus on uniform Cartesian sampling, which is used in a majority of clinical applications. In this scenario, I-subproblem (Eq. [5]) becomes equivalent to the model proposed in Ref. (26): prior information regularized SENSE. Similar to the approach used in conventional SENSE, Eq. [5] can be easily solved using Eq. [6] in Ref. (26) with the same reconstruction time as the conventional SENSE using a pixel-by-pixel approach. In the first iteration, if there is no prior $\hat{I}$ information available from an extra scan, I-subproblem is simply the conventional SENSE. To adopt the noise correlation among coil elements, the sensitivity maps and the acquired data should be adjusted using $\Lambda^{-1/2}V^H$, where Λ and V are the matrices of eigenvalues and eigenvectors of the noise covariance matrix. For both conventional SENSE (1) and prior information regularized SENSE (26), the noise decorrelation is a routine step.

When a Cartesian trajectory is used, model [4] can be further improved by introducing spatially adaptive weights to the regularization term. As the g-factor map (1) is available from the initial I-subproblem, this noise distribution information can be used to improve the effectiveness of $\hat{I}$-subproblem. Because the noise is unevenly distributed in the image I, constant λ values cannot optimally balance the needs for denoising and data fitting at all locations. In a region with a higher noise level, a larger regularization parameter is preferred to remove sufficient noise. Similarly, in a region with a lower noise level, a smaller regularization parameter is ideal to preserve the spatial resolution. A g-factor map, which can be easily calculated for SENSE (1) and Generalized autoclibrating partially parallel acquisitions (GRAPPA) (27), provides the predicted noise distribution information. Hence, a g-factor map is used to define the spatially adaptive regularization parameter to balance the need for sparsity constraints and data fidelity. Based on this idea, Eq. [4] becomes

$$E(I,\hat{I}) = \sum_{j=1}^{\text{Nch}} \left\|F_p(S_jI) - k_j\right\|_2^2 + \lambda\left\|(g-1)\nabla\hat{I}\right\|_1 + \mu\left\|(g-1)\Psi(\hat{I})\right\|_1 + \alpha^2\left\|I - \hat{I}\right\|_2^2, \quad [8]$$

where g is the point-wise g-factor value from the initial I-subproblem. If the g-factor value is close to 1 in a certain region, it means that the noise level is not amplified

by the SENSE reconstruction. Therefore, a limited or no sparsity constraint should be applied to that region to preserve the spatial resolution. Accordingly, $g - 1$, instead of g, is used in [8], and $\hat{I}$-subproblem becomes

$$\hat{I}\text{-subproblem: } \min_{\hat{I}} E|I = \min_{\hat{I}} \lambda\left\|(g-1)\nabla\hat{I}\right\|_1 + \mu\left\|(g-1)\Psi(\hat{I})\right\|_1 + \left\|I-\hat{I}\right\|_2^2. \quad [9]$$

The numerical method provided in Ref. (12) is used to solve [9]. The fast numerical method works well for complex images. Hence, both magnitude and phase will be denoised through [9]. The point-wise g-factor values bring no extra computational costs for solving [9] compared to [7].

Joint estimation of sensitivity maps and reconstructed image (JSENSE) has been proposed (28,29) to further reduce reconstruction errors by using updated sensitivity maps. This idea is adopted in this algorithm. Sensitivity maps can be updated after $\hat{I}$-subproblem. Let $\hat{I}$ denote the initial result of $\hat{I}$-subproblem. To improve the accuracy of the sensitivity maps, $\hat{I}$ is projected back into k-space channel-wise using initial sensitivity maps. If the central k-space data is fully acquired, it can be inserted back to update the reconstructed k-space. Then the sensitivity maps can be recalculated from the complete and updated k-space data sets. If there is no fully acquired central k-space available, then this sensitivity map update step can be skipped. To improve spatial resolution of $\hat{I}$, all acquired data can be inserted back, which can then be combined to produce an improved $\hat{I}$ using sensitivity map-weighted summation (30). For final reconstruction, the updated sensitivity maps and updated $\hat{I}$ can then be used as inputs in [5]. As both the updated sensitivity maps and $\hat{I}$ are available from a self-feeding mechanism, this specific implementation for sparsity-constrained SENSE is named self-feeding Sparse SENSE.

The flowchart shown in Fig. 1 summarizes the method described above. For a better explanation of the procedure for updating calibration information (sensitivity maps and $\hat{I}$), Fig. 2 uses an example to show the details. The acquisition scheme of the data used in this example will be provided in the Methods section. For better visualization, Fig. 3 shows some enlarged images from Fig. 2. With low-resolution sensitivity maps (Fig. 3b), the initial reconstruction (Fig. 3c) of I-subproblem by conventional SENSE could contain a significantly high noise/artifact level when the acceleration factor is high. In this example, the acceleration factor was 5. $\hat{I}$-subproblem using [9] results in an image, $\hat{I}$, with a reduced noise and artifact level, but also with a reduced spatial resolution (Fig. 3d). By substituting with the acquired k-space, an image, $\hat{I}$, with higher spatial resolution and low noise/artifact level can be generated (Fig. 3e). Similarly, improved sensitivity maps (Fig. 3f) can be generated.

Parameter Decision Scheme

There are three regularization parameters in the whole procedure: α in [5] for I-subproblem, which balances the data fidelity and image similarity between I and $\hat{I}$ and λ and μ in Eq. [9] for $\hat{I}$-subproblem, which balance image smoothing and signal preservation.

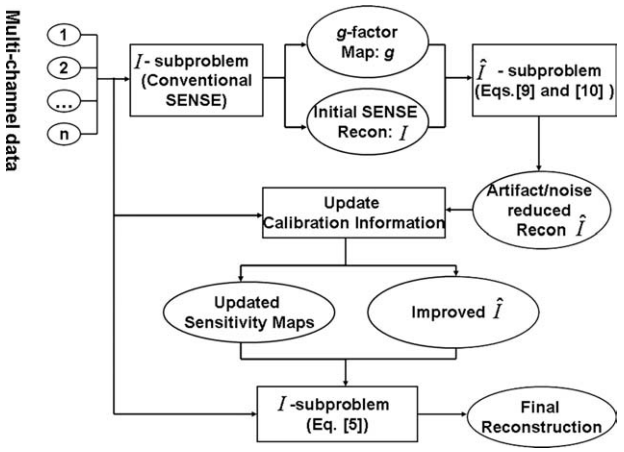

FIG. 1. Flowchart of the proposed self-feeding Sparse SENSE, a specific implementation of the variable splitting and quadratic penalty technique for Cartesian data sets. Because the inputs for the final reconstruction step are from a self-feeding mechanism, this implementation is called self-feeding Sparse SENSE.

According to the deduction from Eq. [4], α should be sufficiently large. In a self-feeding Sparse SENSE, $\hat{I}$ is the result of image denoising from the reconstruction of a previous iteration by $\hat{I}$-subproblem. It is a close approximation of the true image but potentially with lower spatial resolution. With the expectation that the reduction of spatial resolution is limited due to optimal λ and μ; α is fixed to be 0.5 in all experiments.

Based on our experience and reports in (7), it is found that, if the wavelet transform is used, the optional sparsity term $\|\Psi(I)\|$ does not contribute much to the final reconstruction. For simplicity, this optional term is turned off by fixing $\mu = 0$. As the overall noise level in the reconstructed image is related to the values in the g-factor map, the regularization scalar λ is defined by the mean of g-factor. A high mean g-factor value indicates a high overall noise level, therefore, a large λ should be used. Consequently, λ is defined to be

$$\lambda = \text{mean}(g) \times 0.01. \quad [10]$$

Here *mean*(*) is the operator to calculate mean in the image support or region of interest. An empirical value, 0.01, is proposed for scaling. Using [9] and [10], the weight of sparsity constraint term is automatically defined by the g-factor. If mean (g) is very close to 1, the initial SENSE reconstruction can be used as the final result to avoid prolonged reconstruction time due to further steps. More clarification on the values of α and the scalar in [10] will be provided in Restults and Discussion sections.

Beside the regularization parameters, there is one extra parameter for the number of iterations of sub-problems [5] and [9]. As shown in Fig. 1, self-feeding Sparse SENSE processes [5] and [9] only one time after the initial SENSE reconstruction. This is because we found that using more iterations did little to improve the image quality, but increased the reconstruction time in the case of brain imaging. It is possible, however, that more iterations are necessary for some other applications. In this particular work, we used only one iteration in all experiments. The

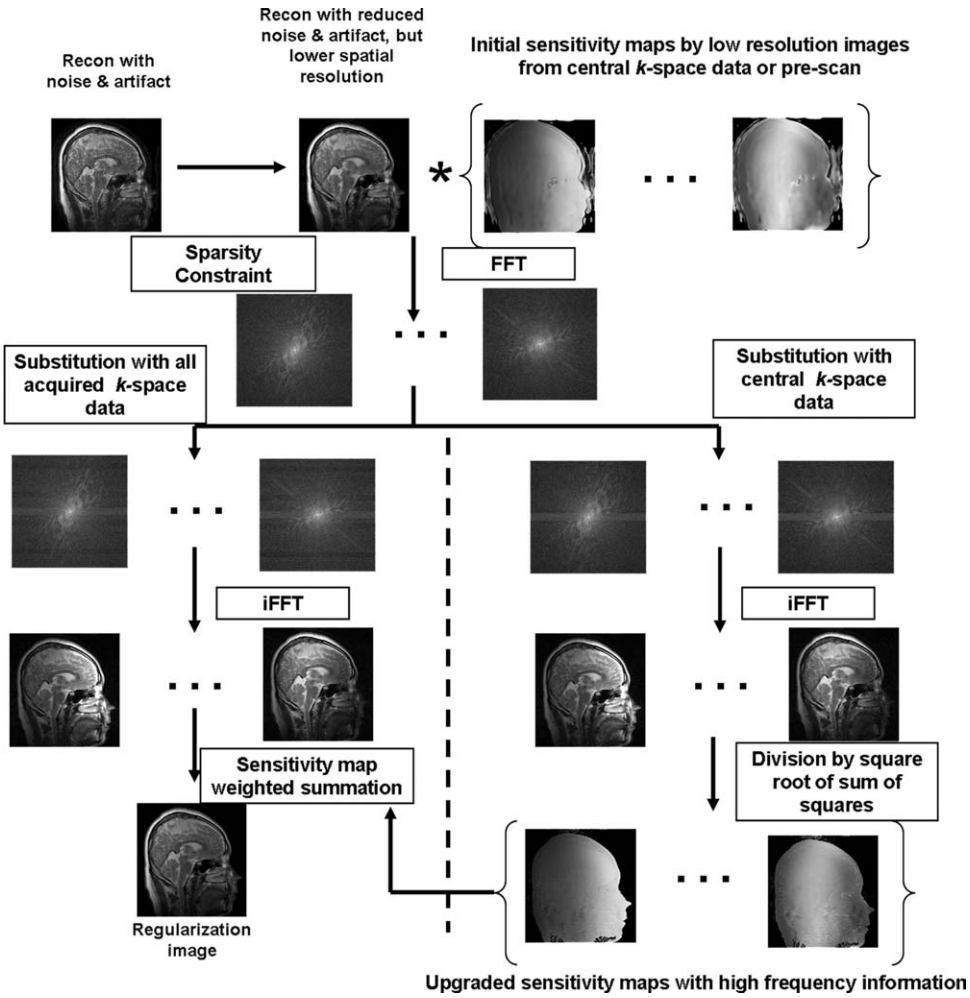

FIG. 2. Flowchart for updating calibration information: sensitivity maps and $\hat{I}$. Left and right side of the dashed line denote the improvement of $\hat{I}$ and sensitivity maps, respectively.

updating of sensitivity maps and the efficiency of SENSE for unfolding contribute to the fast convergence.

METHODS

Data Acquisition

Experiments were designed to evaluate whether the proposed method could consistently produce high quality images with high acceleration factors in a reasonable time period. Two brain data sets were acquired using a 3.0-T Philips scanner (Philips, Best, Netherlands) using T2-weighted turbo spin echo (T2 TSE) and T1-weighted gradient echo imaging (T1 FFE) sequences. In addition, low-resolution pre-scans were acquired to produce pre-scanned sensitivity maps. Both bodycoil and phased array coil were used for the pre-scans. All data sets were fully acquired using commercially available eight-element head coils (Invivo Corp, Gainesville, FL, USA), and then artificially down-sampled for reconstruction. Table 1 provides the acquisition parameters for these data sets. The data set acquired by T2 TSE (data set 1) was used for Figs. 2 and 3.

Implementation of Algorithms

Eqs. [5] and [9] were used to implement the proposed self-feeding sparse SENSE. Eq. [6] in Ref (26) was used to solve I-subproblem (Eq. [5]) through a pixel-by-pixel approach. Initially, since there was no $\hat{I}$ available, conventional SENSE was used. The initial sensitivity maps could be either from the self-calibration signal or from pre-scan. The outputs of the conventional SENSE, both the g-factor map and the reconstructed image, were used as inputs of $\hat{I}$-subproblem (Eq. [9]). As mentioned in the Theory section, $\alpha = 0.5$, $\lambda = \text{mean}(g) \times 0.01$, and $\mu = 0$ were used in all experiments. Also, only one iteration was used after the initial SENSE reconstruction, as shown in Fig. 1.

For comparison, a conjugate gradient (CG)-based solution to Eq. [1], Conjugate Gradient-Compressed Sensing SENSE (CS SENSE), was also implemented. In this work, $\mu = 0$ was used for CG-CS SENSE. Instead of a fixed λ, the optimal regularization parameter was manually tuned for CG-CS SENSE. Also, the termination of CG-CS SENSE was manually controlled to achieve the lowest error with the least number of iteration. The initial input for conjugate gradient iteration was the result of conventional SENSE. Data set 1 was used for experiments with self-calibrated sensitivity maps. To use the self-calibration signal in the final reconstruction, the result of Eq. [5], $\hat{I}$, was projected back into k-space channel-wise after multiplication with sensitivity maps. The central k-space data was inserted back to update the reconstructed k-space. Then the final reconstruction was produced using Romer's combination scheme (30). In the

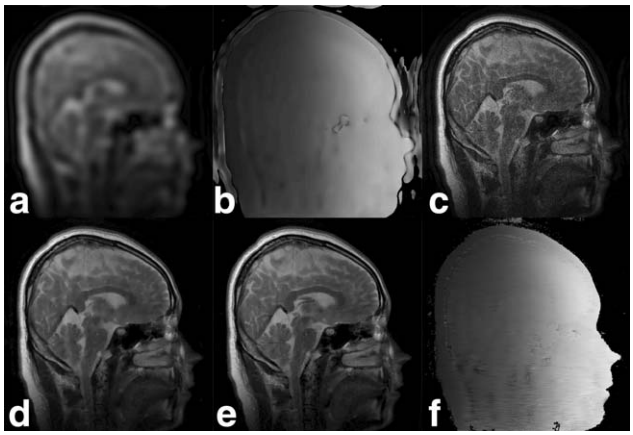

FIG. 3. Some enlarged images in Fig. 2. (**a**) Composite image from the 32 central *k*-space lines for initial sensitivity map calculation; (**b**) initial sensitivity map of channel 1 using the 32 central *k*-space lines, (**c**) initial reconstruction of *I*-subproblem through conventional SENSE, (**d**) result of $\hat{I}$-subproblem using Eq. [9] showing a reduced noise/artifact level than (c); (**e**) improved $\hat{I}$, which is the result after the substitution of all acquired *k*-space data with higher spatial resolution than (d); (**f**) updated sensitivity maps. Figure 3e,f will be used as inputs for *I*-subproblem.

implementation of GRAPPA, the size of the convolution kernel was 4 × 5. The data set acquired by T1 FFE sequence (data set 2) was used for experiments using prescanned sensitivity maps. The prescanned low-resolution images were only used for sensitivity map calculation. In short, the proposed methods were compared with CG-CS SENSE, conventional SENSE, and GRAPPA.

Design of Experiments

To compare the proposed method with other existing methods when the sensitivity maps were self-calibrated, data set 1 was reconstructed with nominal undersampling factors of 2, 3, 4, and 5 by SENSE, GRAPPA, CG-CS SENSE, and the proposed method. The 32 central *k*-space lines were used for initial sensitivity map calculation and the final reconstruction. Hence the net acceleration factors were 1.9, 2.6, 3.4, and 4, respectively.

To test the performance of the proposed method for data sets with pre-scanned sensitivity maps, data set 2 was used. Net acceleration factors 4 and 5 were used in the artificial down sampling. The results of conventional SENSE were used for comparison.

Accuracy, speed, and robustness were all considered for comparison. For accuracy assessments, both the magnitude and the distribution of the error were measured. As full *k*-space data was available, the image reconstructed with the full *k*-space data was used as the reference image. The root mean square error (RMSE) was used to evaluate the overall magnitude of error. The error map depicts the distribution of the difference in magnitudes between the reconstruction and the reference and was used to show error distribution. The zoomed-in image was used to demonstrate the preservation of fine structures and sharp edges.

Robustness refers to the insensitivity of the reconstruction to the choice of parameters. In each of the experiments above, all the parameters of the proposed method were automatically defined. To demonstrate the rationale of the choice of parameters, two set of experiments using the proposed method were processed with a wide range of parameters. In one set of experiment, the λ was defined by Eq. [10], and α was changed from 0 to 4 gradually. In the other experimental set, α was fixed to be 0.5 and the scalar in Eq. [10] was changed from 0 to 0.1 gradually. RMSEs were recorded for each set of parameters. Net acceleration factor 4 was used for all data sets in this set of experiments.

All methods were implemented using the MATLAB® programming environment (MathWorks, Natick, MA). The MATLAB® codes were processed on a Dell Precision Laptop (Dell, Round Rock, TX) with dual 2 GHz processors and 3.25 GB RAM.

RESULTS

Figure 4–6 illustrate the comparison of the proposed self-feeding sparse SENSE with other reconstruction methods using data set 1. Error maps (Fig. 4), zoomed-in regions of the reconstructed images (Fig. 5), and the plot of RMSEs (Fig. 6) were used for comparison. Self-calibrated sensitivity maps were used for reconstruction. From the error maps in Fig. 4, it can be seen that the reconstruction by the proposed method (Fig. 4b) has the lowest error level. The spatial resolution was only slightly reduced at regions with high noise levels in the SNESE reconstruction (Fig. 4c). The results by SENSE and GRAPPA (Fig. 4d) clearly showed a higher noise level than Fig. 4b. Figure 4e,f show the sensitivity of CG-CS SENSE to the choice of regularization parameter. When $\lambda = 0.04$, serious residual noise can be observed (Fig. 4e). When λ was tuned to 0.08, boundaries of the brain structures can be observed (Fig. 4f). This means that the spatial resolution of the image was damaged. In our experiments, it was extremely difficult to find an optimal λ for well-balanced spatial resolution preservation and SNR improvement for CG-CS SENSE. In Fig. 5, zoomed-in images were used to show the comparison. Compared to Figs. 5c–f, the reconstruction by the

Table 1
Data Acquisition Parameters

Data Set Serial number		Sequence	FOV (mm^2)	Matrix size	TR/TE (ms)	ETL or TI	PE direction
1		T2 TSE	205	500 × 512	3000/85	ETL 20	AP
2	Prescan	T1 FFE	230	96 × 96	250/20		LR
	Imaging	T1 FFE	230	320 × 320	250/4.1		LR

AP, anterior-posterior; ETL, echo train length; FOV, field of view; LR, left-right; PE, phase encoding; TE: echo time.

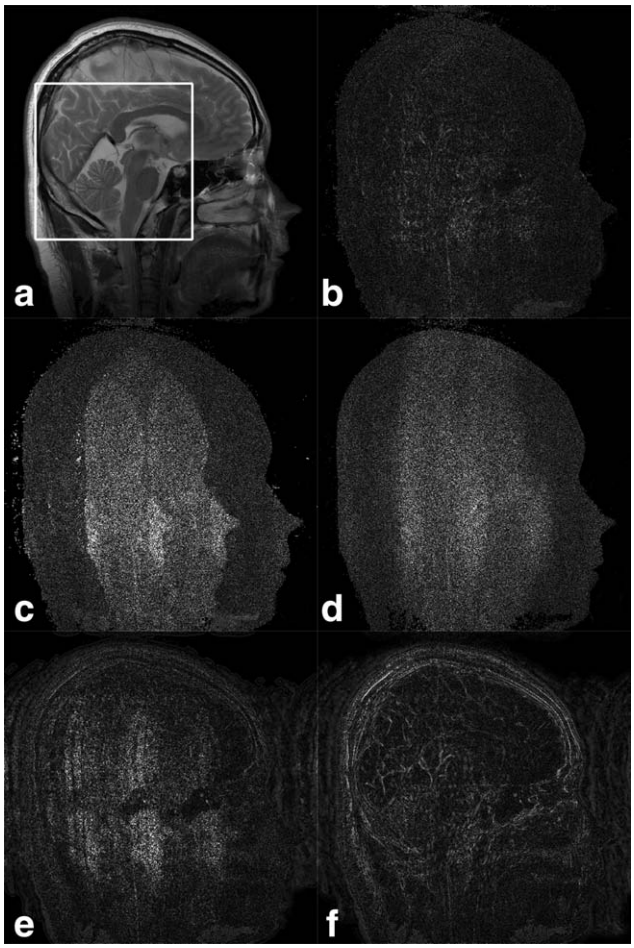

FIG. 4. Comparison using error maps from data set 1 with an acceleration factor of 5. **a**: The reference image. The white box defines the zoomed in region shown in Fig. 5. (**b–f**) are the error maps of the reconstruction by the proposed method (b), SENSE (c), GRAPPA (d), CG-CS SENSE with $\lambda = 0.04$ (e), and CG-CS SENSE with $\lambda = 0.08$ (f), respectively. The same intensity scale was used for all these error maps. The RMSEs of the reconstructions corresponding to (b–**g**) are 8.1, 20.3,17.1, 12.8, and 10.4%.

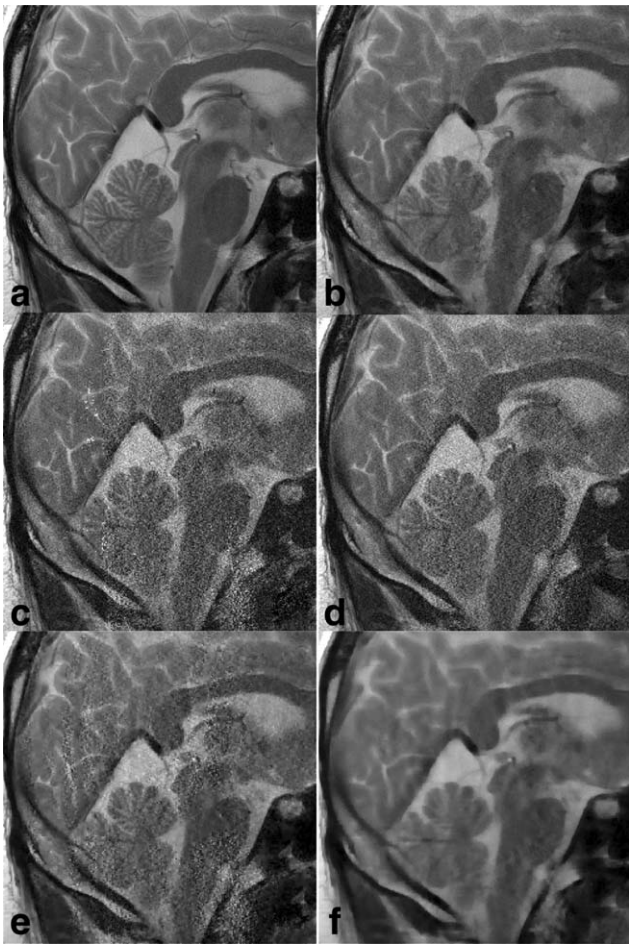

FIG. 5. Comparison using zoomed in images with data set 1. The zoomed in region is defined by the white box in Fig. 4a). The acceleration factor was 5. **a–f**: are the reference image (a), the reconstruction by the proposed method (b), SENSE (c), GRAPPA (d), CG-CS SENSE with $\lambda = 0.04$ (e), and CG-CS SENSE with $\lambda = 0.08$ (f), respectively.

proposed method (Figs. 5b) clearly has better balance of preservation of spatial resolution and SNR improvement. Figure 6 plots the comparison of RMSEs of several reconstruction methods at different acceleration factors. For the RMSE values of CG-CS SENSE, the lowest value among results by different regularization parameters was used. When the acceleration factor was 4 and 5, the RMSEs of the results by the proposed method were significantly lower than those by other reconstruction methods.

Table 2 compares the reconstruction time for this data set as well as presenting the values of the optimal λ for CG-CS SENSEN. The last column provides the mean of the *g*-factor values in initial SENSE reconstruction, which was used to automatically define the regularization weight of self-feeding Sparse SENSE through Eq. [10]. Note that the time for the proposed self-feeding Sparse SENSE included the time for sensitivity maps calculation and *g*-factor map calculation. The number of iterations of CG-CS SENSE was manually controlled to minimize the reconstruction time for optimal results. From Table 2 it can be seen that the optimal λ for CG-CS SENSE changed greatly for different acceleration factors. Also, even using a manual control scheme, when the

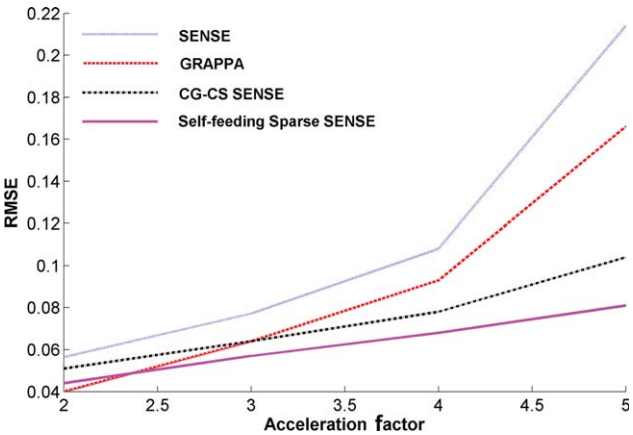

FIG. 6. Plot of RMSEs of reconstructions at different acceleration factors.

Table 2
Comparison of Reconstruction Time and Parameters for a 500 × 512 × 8 Data Set

SENSE		CG-CS SENSE			Self-feeding Sparse SENSE	
R	Time	Time	λ	Nit	Time	Mean (*g*)
2	27	153	0.01	5	57	1.12
3	19	506	0.04	15	42	1.48
4	16	446	0.05	15	34	2.3
5	12	373	0.08	20	26	3.7

Time is in seconds. Mean (*g*) is the mean of *g*-factor values. Nit is the number of iterations.

acceleration factor was greater than 2, the reconstruction time of CG-CS SENSE was still more than 10 times longer than when using the proposed method.

Figure 7 shows the results with pre-scanned sensitivity maps. The spatial resolution of the pre-scan was 96 × 96. For comparison, the results for conventional SENSE are also presented. The total processing time using the proposed method for this 320 × 320 × 8 data set was 13.2 sec. Even at a net acceleration factor of 5, the vessel is well defined in the reconstruction (Fig. 7g). From the difference map (Fig. 7e), it can be seen that the spatial resolution was not obviously impacted when the net acceleration factor was as high as 4. Compared with the result using conventional SENSE, the RMSE was reduced from 13.2 to 6.4%.

Figure 8 shows the plots of RMSEs with respect to different regularization parameters. Figure 8a depicts the change with respect to regularization parameter α in *I*-subproblem. Figure 8b depicts the change with respect to the scalar in Eq. [10] for the definition of regularization parameter λ for $\hat{I}$-subproblem. It can be seen that fixed values used in this work provided RMSE close to the lowest. Notice that, in addition to RMSE, spatial resolution is another important criterion. Therefore, conservative values (moderate regularization parameters) were used to preserve spatial resolution. Figure 8 demonstrates why 0.5 and 0.01 were used for α and scalar, respectively, in Eq. [10].

DISCUSSION

Advantages of the Proposed Method

When compared with the conjugate gradient-based sparsity-regularized SENSE, the proposed method is much faster. The computational cost for the proposed method is two conventional SENSE reconstructions plus one spatially adaptive image denoising procedure. Regardless of the number of channels, this denoising step only took ~1 sec for a 256 × 256 image, and ~4 sec for a 512 × 512 image. When the acceleration factor was 4, the total processing time for a 256 × 256 × 8 data set and for a 500 × 512 × 8 data set was 9.7 and 36 sec, respectively, using the MATLAB® environment. In contrast, the CG-CS SENSE took 446 sec for the 500 × 512 × 8 data set (Table 2). This difference in speed can be explained by the decomposition of the original complex problem into two much simpler subproblems. For an equally spaced Cartesian trajectory, which is the most commonly used trajectory in clinical applications, *I*-subproblem can be solved with the same reconstruction time as conventional SENSE, which has computational complexity $O(N \times R^2)$, N being the number of pixels of the image and R the acceleration factor. $\hat{I}$-subproblem is simply one of a number of image denoising problems that have been intensely studied during the past decades (12,18,19,21–25). Fast and robust numerical methods can easily be found in the literature. In this work, the method in Ref. (12) was used. Beside four steps that have computational complexity O(N), the most expensive computation in each iteration for $\hat{I}$-subproblem is two fast Fourier transforms (FFT). To the contrary, the number of FFTs in each iteration of CG-CS SENSE is 4 × Nch, as the fidelity term uses data from all channels. Moreover, the computational complexity to find the optimal step size in each iteration is $O(N \times \text{Nch} \times R^{-1}) \times \text{Ntry}$, where Ntry is the number of tests for optimal step size. Therefore, for each iteration, CG-CS SENSE needs 4 × Nch − 2 more FFTs than $\hat{I}$-subproblem, and significantly more effort to reach optimal step size. Another reason for fast reconstruction speed of the proposed method is that a single iteration after the initial SENSE reconstruction turned out to be

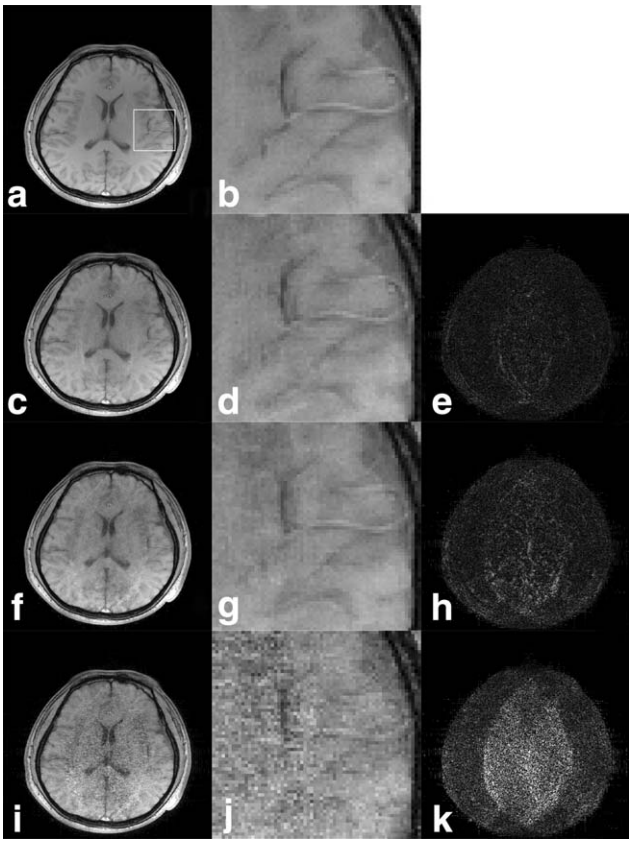

FIG. 7. Reconstruction with pre-scanned sensitivity maps (96 × 96). **a**: The reference image, (**c**), and (**f**) are the reconstructions by the proposed method at net acceleration factors 4 and 5, respectively; (**i**) is the reconstruction by SENSE at net acceleration factor 5. The RMSEs of c), f), and i) are 4.4, 6.4, and 13.2%. Figure 7**b**, **d**, **g**, and **j** demonstrate the corresponding enlarged region defined by the white box in a. Figure 7**e**, **h**, and **k** are difference maps of c, f, and i. The difference maps were brightened five times.

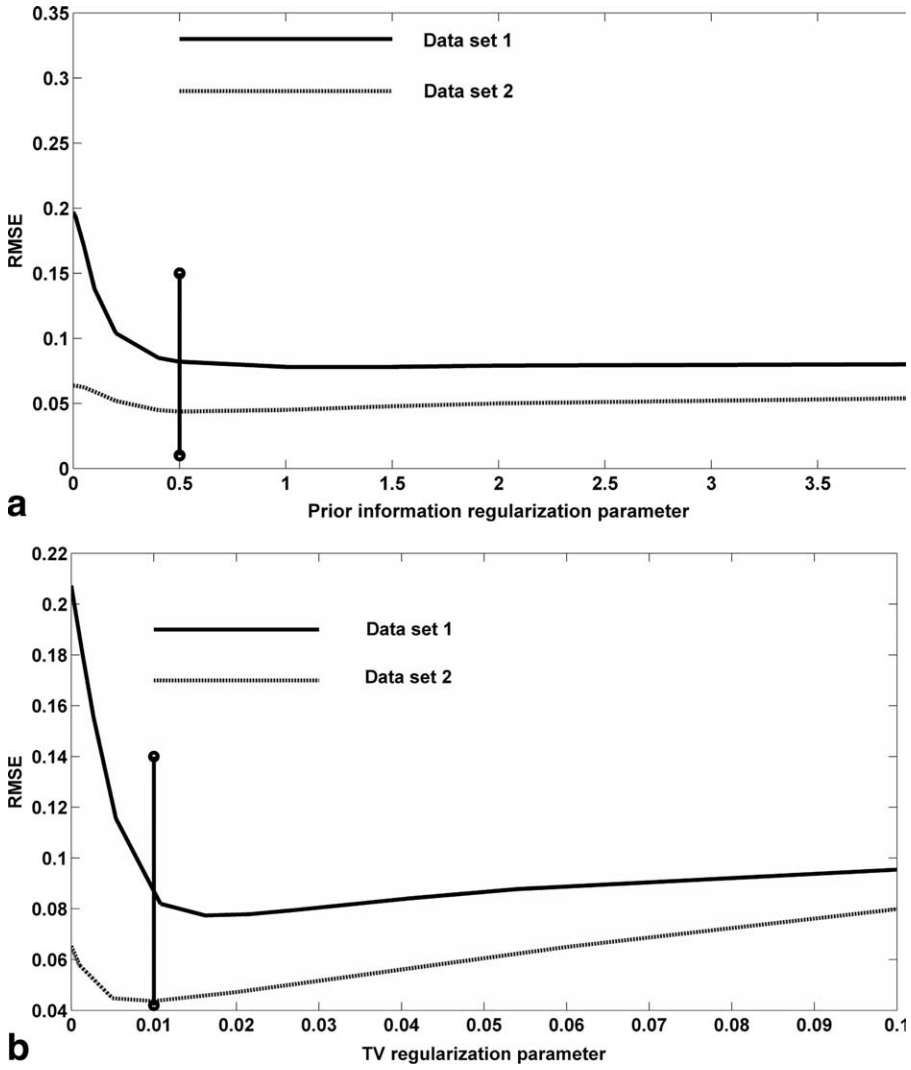

FIG. 8. Plots of RMSEs with respect to the regularization parameters. **a**: RMSE against α in Eq. [5]. The scalar in Eq. [9] was fixed at 0.01. **b**: RMSE against the scalar in Eq. [9]; α was fixed at 0.5. The vertical lines show the values used in this article.

sufficient. The updated sensitivity maps and the strength of SENSE in unfolding the undersampled data significantly increase the speed of convergence.

Another advantage of the proposed self-feeding Sparse SENSE is that this method provides a good balance between the preservation of spatial resolution and the reduction of noise. Compared with conventional PPI techniques, the RMSE is dramatically reduced when the acceleration factor is high. Meanwhile, from the difference maps and zoomed-in images, it can be seen that the cost of spatial resolution for SNR improvement is minimal. This advantage is due to the spatially adaptive regularization technique used in $\hat{I}$-subproblem. The *g*-factor map is used to define the spatially adaptive regularization parameter. This offers the potential to sufficiently remove noise in regions with higher noise levels, meanwhile preserving as much as possible spatial resolution in regions with lower noise levels. With a constant regularization parameter, this is very difficult, if not impossible. As shown in Figs. 4e and 5e, severe residual noise can be observed in regions with a high noise level when a small constant, 0.04, was used. When a larger constant, 0.08, was used, the noise was removed at the cost of a significant reduction in spatial resolution. Image structures can be clearly observed in the error map (Fig. 4f). It should be noted that a conventional acquisition scheme, Cartesian and equally spaced phase encoding lines, was used in our experiments. CG-CS SENSE prefers random or pseudo-random acquisition to produce more evenly distributed noise and thus avoids the need for weighted smoothing. With an optimal acquisition scheme, CG-CS SENSE can potentially produce more accurate results than those obtained using a conventional acquisition scheme. However, the optimal acquisition scheme might be difficult to implement in general applications.

Besides speed and accuracy, robustness is another advantage of the proposed method. In all these experiments, the same set of parameters ($\alpha = 0.5$, λ as defined by Eq. [10]) was used. The reconstructions used both self-calibrated and pre-scanned sensitivity maps with a wide range of acceleration factors (from 2 to 5). The same set of parameters consistently produced images with well-balanced SNR and spatial resolution. Figure 8 further demonstrates the relationship between the parameters and RMSE. Figure 8a demonstrates that the RMSE would be stable once $\alpha > 1$. This is reasonable since the reconstruction will converge on the output of $\hat{I}$-subproblem when α increases. A small value for α will

make the reconstruction rely more on the conventional SENSE, which potentially has a low SNR when the acceleration factor is high. As the output of $\hat{I}$-subproblem has a high SNR, but potentially a lower spatial resolution, a moderate value of 0.5 was used in our experiments to preserve spatial resolution. The vertical line in Fig. 8a shows the location. A smaller λ means less smoothing in $\hat{I}$-subproblem, and potentially results in an image with some residual noise and well preserved spatial resolution. A larger λ gains SNR at the cost of spatial resolution. It was noticed that the lowest RMSE was achieved when the scalar in Eq. [10] was around 0.01 (between 0.005 and 0.015) for all data sets. Hence 0.01 was used in our work. The results show that the fixed scalar worked well for all acceleration factors. This is different from CG-CS SENSE. In Table 2, it can be seen that the optimal λ changes from 0.01 to 0.08 for acceleration factors 2 to 5, respectively.

In summary, a rapid and robust numerical algorithm has been proposed for sparsity-constrained parallel imaging using the conventional Cartesian acquisition scheme. Acceleration factors higher than conventional PPI techniques can be achieved with minimal impact on image resolution and SNR.

Future Work

In this work, RMSE was used to quantitatively evaluate image quality. While RMSE cannot sufficiently show the preservation diagnostic information, a necessary future project is to clinically evaluate the proposed method.

The introduction of the auxiliary variable decomposes the sparsity constrained PPI energy functional into two subproblems. The two corresponding equations ([5] and [7]) are applicable to acquired data sets with any trajectory. In this work, a specific implementation with Cartesian trajectory is introduced. The framework can be easily extended to non-Cartesian data sets or non-SENSE PPI techniques. For example, using a prior information regularized GRAPPA technique (31) and its extension for a radial data set (32), this framework can be easily adopted for sparsity constrained radial GRAPPA. Given a fast numerical method for Eq. [5] with arbitrary trajectory, the proposed method can be extended to all trajectories. Fortunately, one recent improvement in mathematics (33) provides a simple, but very efficient, approach to Eq. [5] with arbitrary trajectory. In conjunction with GRAPPA operator gridding (GROG) (34), used to avoid gridding in iteration, preliminary results show that, when matrix size is $256 \times 256 \times 8$, sparsity-constrained SENSE with arbitrary trajectories can be finished in 15 sec (35). Additional results for data sets with arbitrary trajectories will be reported separately in the future.

It is possible that more iterations or better parameter settings can further improve reconstruction accuracy. However, for brain imaging, more iterations did little to improve reconstruction accuracy. To avoid a longer reconstruction time, the current version of self-feeding Sparse SENSE does not adopt an iterative reconstruction scheme. In the future, the potential benefit of iterative reconstruction on other applications will be studied. Also, two empirical values, based on Fig. 8, were used for regularization parameters. In addition to those shown in this article, in all our experiments, these values consistently generated images with well-balanced SNR and spatial resolution. Also, it is possible to further optimize these parameters. In just one example, α can be spatially adaptive based on the spatially different reliability of $\hat{I}$. In regions with a *g*-factor value close to 1, no sparsity regularization is applied. Hence the reliability of these regions should be higher than regions with high *g*-factor values. Future results with more discussion will be reported.

Some comparisons on accuracy and speed were presented in this work. Numerous advanced methods (4,5,8,9) on sparsity-constrained PPI have been recently published. Because of the limited amount of information provided in these publications, it is hard to compare these techniques with the proposed method. In the future, we would like to further compare speed, accuracy, and robustness of this method with others.

CONCLUSIONS

It is demonstrated that the conventional sparsity-constrained PPI can be decomposed into two simpler subproblems, each of which can be solved in a much faster and robust manner. Using spatially adaptive regularization combined with a Cartesian trajectory, the proposed self-feeding Sparse SENSE method can robustly produce images with well-balanced SNR and spatial resolution at high acceleration factors.

REFERENCES

1. Pruessmann KP, Weiger M, Scheidegger MB, Boesiger P. SENSE: Sensitivity encoding for fast MRI. Magn Reson Med 1999;42:952–962.
2. Griswold MA, Jakob PM, Heidemann RM, Mathias Nittka, Jellus V, Wang J, Kiefer B, Haase A. Generalized autocalibrating partially parallel acquisitions (GRAPPA). Magn Reson Med 2002;47:1202–1210.
3. Block K, Uecker M, Frahm J. Undersampled radial MRI with multiple coils: iterative image reconstruction using a total variation constraint. Magn Reson Med 2007;57:1086–1098.
4. Liang D, King KF, Liu B, Ying L. Accelerating SENSE using distributed compressed sensing. Proc Intl Soc Mag Reson Med 17; Honolulu, Hawaii; 2009. p 377.
5. Lusting M, Alley M, Vasanawala S, Donoho DL, Pauly JM. L1 SPIRiT: autocalibrating parallel imaging compressed sensing. Proc Intl Soc Mag Reson Med 17; Honolulu, Hawaii; 2009. p 379.
6. King KF. Combining compressed sensing and parallel imaging. Proc Intl Soc Mag Reson Med 16; Toronto, Canada; 2008. p 1488.
7. Lustig M, Donoho D, Pauly JM. Sparse MRI: The application of compressed sensing for rapid MR imaging. Magn Reson Med 2007;58:1182–1195.
8. Fernandez-Granda C, Senegas J. L1-norm regularization of coil sensitivities in non-linear parallel imaging reconstruction. Proc Intl Soc Mag Reson Med 17; Honolulu, Hawaii; 2009. p 380.
9. Fischer A, Seiberlich N, Blaimer M, Jakob P, Breuer F, Griswold M. A combination of nonconvex compressed sensing and GRAPPA (CS-GRAPPA). Proc Intl Soc Mag Reson Med 17; Honolulu, Hawaii; 2009. p 2813.
10. Doneva M, Eggers H, Rahmer J, Bornert P, Mertins A. Highly undersampled 3D golden ratio radial imaging with iterative reconstruction. Intl Soc Mag Reson Med 16; Toronto; 2008. p 336.
11. Huang F, Chen Y. Self-adjusted regularization ratio for robust compressed sensing. Intl Soc Mag Reson Med 17; Hawaii; 2009, p. 4592.
12. Yang J, Zhang Y, Yin W. A fast TVL1-L2 minimization algorithm for signal reconstruction from partial Fourier data: IEEE Journal of Selected Topics in Signal Processing, 2009;4:288–297.

13. Osher S, Mao Y, Dong B, Yin W. Fast linearized Bregman iteration for compressive sensing and sparse denoising. Commun Math Sci 2010;8;93–111.
14. Donoho DL, Elad M, Temlyakov V. Stable recovery of sparse overcomplete represenation in the presence of noise. IEEE Trans Inf Theory 2006;52:6–18.
15. Ye X, Chen Y, Huang F. MR image reconstruction via sparse representation: modeling and algorithm. The 2009 International Conference on Image Processing, Computer Vision, and Pattern Recognition (IPCV′09); July 13–16, 2009; Las Vegas. pp 10–16.
16. Kim S, Koh K, Lustig M, Boyd S. An efficient method for compressed sensing. IEEE Intl Conf Image Process (ICIP); Sep 16–19, 2007; San Antonio, Texas, USA; pp 117–120.
17. Chang T, He L, Fang T. MR image reconstruction from sparse radial samples using Bregman iteration. Intl Soc Mag Reson Med 14; Seattle, WA; 2006. p 696.
18. Cai JF, Osher S, Shen Z. Linearized Bregman iterations for compressed sensing: UCLA; 2008. Report nr CAM 08-06.
19. Osher S, Mao Y, Dong B, Yin W. Fast linearized Bregman iteration for compressive sensing and sparse denoising: UCLA; 2008. Report nr CAM 08-37.
20. Yin W, Osher S, Goldfarb D, Darbon J. Bregman iterative algorithms for L1-minimization with applications to compressed sensing. SIAM J Imaging Science 2008;1:143–168.
21. Goldstein T, Osher S. The split Bregman method for L1 regularized problems. SIAM J Imaging Sci 2009;2:323–343.
22. Guo W, Huang F. Adaptive total variation based filtering for MRI images with spatially inhomogeneous noise and artifacts. International Symposium on Biomedical Imaging, Boston, MA; 2009, 101–104.
23. Wang Y, Yang J, Yin W, Zhang Y. A new alternating minimization algorithm for total variation image reconstruction. SIAM J Imaging Sci 2008;1:248–272.
24. Vijayakumar S, Huang F, Akao J, Duensing GR. g-factor guided denoising for SENSE reconstructed MR images with edge restoration. Intl Soc Mag Reson Med 14; Seattle, Washington; 2006. p 2357.
25. Rudin LI, Osher S, Fatemi E. Nonlinear total variation based noise removal algorithms. Phys D 1992;60:259–268.
26. Lin F-H, Kwong KK, Belliveau JW, Wald LL. Parallel imaging reconstruction using automatic regularization. Magn Reson Med 2004;51: 559–567.
27. Breuer FA, Blaimer M, Seiberlich N, Jakob PM, Griswold MA. A general formulation for quantitative g-factor calculation in GRAPPA reconstructions. Intl Soc Mag Reson Med 16, Toronto, Canada; 2008. p 10.
28. Uecker M, Hohage T, Block KT, Frahm J. Image reconstruction by regularized nonlinear inversion - joint estimation of coil sensitivities and image content. Magn Reson Med 2008;60:674–682.
29. Ying L, Sheng J. Joint image reconstruction and sensitivity estimation in SENSE (JSENSE). Magn Reson Med 2007;57:1196–1202.
30. Roemer PB, Edelstein WA, Hayes CE, Souza SP, Mueller OM. The NMR phased array. Magn Reson Med 1990;16:192–225.
31. Huang F, Li Y, Duensing GR. A regularization with prior information technique for GRAPPA. Intl Soc Mag Reson Med 16; Toronto; 2008. p 1288.
32. Huang F. Parameter free regularized non-Cartesian GRAPPA. ISMRM Workshop on Non-Cartesian MRI; Sedona, Arizona; 2007. Poster 47.
33. Beck A, Teboulle M. A fast iterative shrinkage-thresholding algorithm for linear inverse problems. SIAM J Imaging Sci 2009;2:183–202.
34. Seiberlich N, Breuer FA, Blaimer M, Barkauskas K, Jakob PM, Griswold MA. Non-Cartesian data reconstruction using GRAPPA operator gridding (GROG). Magn Reson Med 2007;58:1257–1265.
35. Huang F, Chen Y, Ye X. Fast iterative SENSE with arbitrary k-space trajectories. ISMRM Third International Workshop on Parallel MRI; Santa Cruz, CA; 2009.